JOURNAL OF THE ROYAL SOCIETY Interface

J. R. Soc. Interface (2008) 5, 1087–1097
doi:10.1098/rsif.2007.1336
Published online 5 February 2008

Compliance of a microfibril subjected to shear and normal loads

Jingzhou Liu[1], Chung-Yuen Hui[1,*], Lulin Shen[1] and Anand Jagota[2]

[1]Department of Theoretical and Applied Mechanics, Cornell University, Ithaca, NY 14853, USA
[2]Department of Chemical Engineering, Lehigh University, Bethlehem, PA 18015, USA

Many synthetic bio-inspired adhesives consist of an array of microfibrils attached to an elastic backing layer, resulting in a tough and compliant structure. The surface region is usually subjected to large and nonlinear deformations during contact with an indenter, leading to a strongly nonlinear response. In order to understand the compliance of the fibrillar regions, we examine the nonlinear deformation of a single fibril subjected to a combination of shear and normal loads. An exact closed-form solution is obtained using elliptic functions. The prediction of our model compares well with the results of an indentation experiment.

Keywords: compliance; elastica theory; fibrils

1. INTRODUCTION

Recent interest in bio-inspired adhesives has motivated many researchers to fabricate microfibril arrays (Liu & Bhushan 2003; Peressadko & Gorb 2004; Chung & Chaudhury 2005; Crosby *et al.* 2005; Glassmaker *et al.* 2005, 2007; Huber *et al.* 2005; Northen & Turner 2005; Yurdumakan *et al.* 2005; Kim & Sitti 2006; Majidi *et al.* 2006; Aksak *et al.* 2007; Gorb *et al.* 2007; Greiner *et al.* 2007; Varenberg & Gorb 2007) and to study their contact mechanics and adhesion (Jagota & Bennison 2002; Gao *et al.* 2003, 2005; Persson & Gorb 2003; Hui *et al.* 2004; Persson *et al.* 2005; Spolenak *et al.* 2005*a*,*b*; Tang *et al.* 2005; Bhushan *et al.* 2006; Tian *et al.* 2006; Yao & Gao 2006; Chen & Gao 2007). Most of these studies focus on how the interface between the microfibrils and a smooth, hard substrate separates under a normal load. Of equal importance is how these fibrillar surfaces respond to a combination of normal and shear loads. For example, experiments have demonstrated that the maximum shear force a gecko seta can support is approximately six times greater than its normal pull-off force (Autumn *et al.* 2000), and direct measurements of how various species adhere to surfaces are conducted under shear (Irschick *et al.* 1996). However, these observations are often interpreted using theories based on the normal contact of surfaces. Therefore, there is a need to develop contact and adhesion models that take account of shear.

In the past year, there have been several experimental studies on the frictional behaviour of microfibril arrays against a flat substrate (Majidi *et al.* 2006; Ge *et al.* 2007). The fibril arrays fabricated by Majidi *et al.* (2006) and Ge *et al.* (2007) consist of very stiff fibrils, whereas those fabricated by P. R. Guduru (2007, personal communication) and Shen *et al.* (2008) are made of poly(dimethylsiloxane) (PDMS), a soft elastomer with a shear modulus of the order of 1 MPa. Despite the large differences in modulus, what emerges from these experiments is that the static friction of these arrays is much higher than that exhibited by flat unstructured controls made of the same material.

The mechanics of a flat elastic substrate indented by a smooth, soft elastic sphere under a normal load is well described by the Johnson–Kendall–Roberts theory (Johnson *et al.* 1971). A theory for the compliance of microfibril arrays under normal indentation has been developed (Noderer *et al.* 2007). While there is a strong quantitative influence of the fibrillar architecture on compliance, there are qualitative similarities between it and an unstructured flat control. For example, the load versus contact area curves have similar shapes and compliance generally decreases with increasing contact area (increasing load). The situation can be quite different with shear. Figure 1*a* shows schematically an experiment in which a film-terminated PDMS microfibril array is moved in shear relative to a fixed spherical indenter. Briefly (see Shen *et al.* (2008) for details), the microfibril array consists of micropillars oriented normal to an elastic PDMS backing layer. The micropillars are connected at their terminal ends by a thin, flexible film. This structure has been shown to significantly improve adhesion when compared with a flat unstructured control (Glassmaker *et al.* 2007; Noderer *et al.* 2007). The backing layer is bonded to a glass slide that is placed on an inverted optical microscope. Since PDMS is transparent, its deformation can be recorded by the microscope. A fixed normal load, F_N, is applied to press the indenter into contact with the sample surface (i.e. the thin film).

*Author for correspondence (ch45@cornell.edu).

Received 12 December 2007
Accepted 14 January 2008

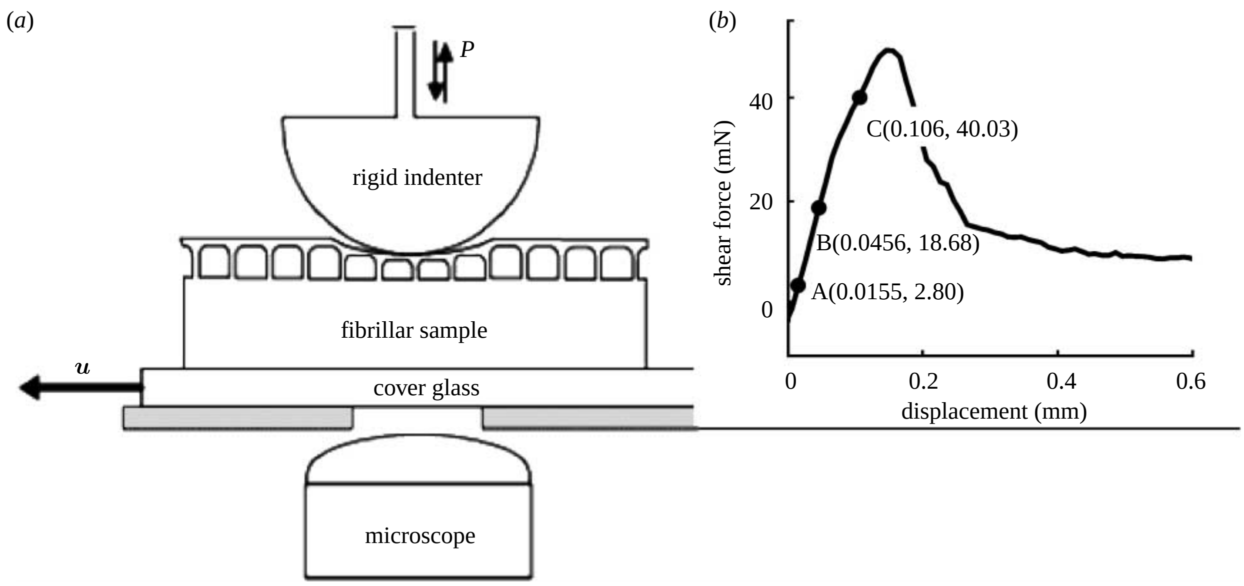

Figure 1. (*a*) A glass spherical indenter is placed on the surface of a microfibril array under a fixed normal force (P) (applied via a mechanical balance). The sample is translated at a constant rate, $\boldsymbol{u}$, and the shear force is measured by a load cell. Deformation near the contact region is recorded by means of an inverted optical microscope. The shear load versus shear displacement curve for a fibrillar sample is shown in (*b*). Three points are selected for comparison with the theory.

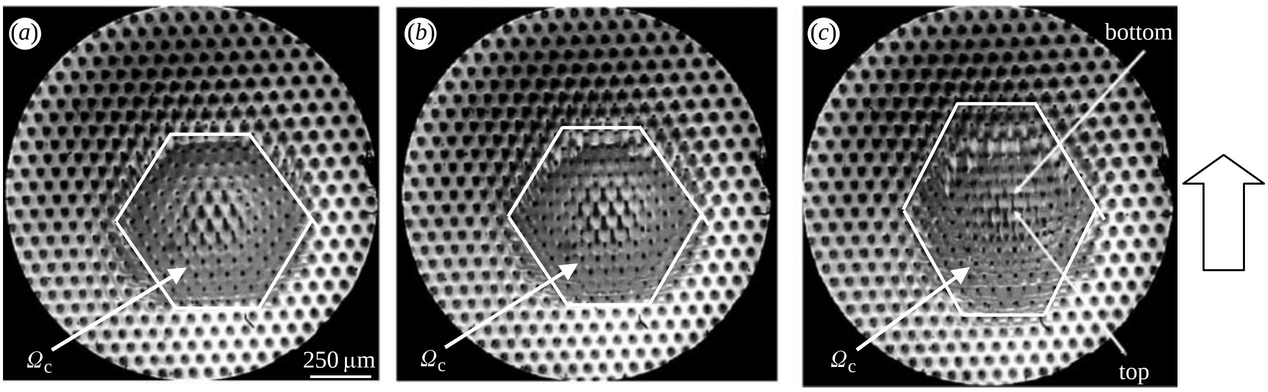

Figure 2. Optical micrographs of the contact region. The direction of shear displacement u is indicated by the arrow on the right. The image of the top end of a fibril appears as a fuzzy grey circle, whereas the bottom end appears as a smaller dark square. This difference allows us to determine the relative deflection Δ_T of each fibril. (*a*–*c*) correspond to the points A–C in figure 1*b*, respectively. The contact region Ω_c is the white polygon.

The shear force F_s is applied by translating the glass slide at a constant rate. A typical shear force versus shear displacement curve is shown in figure 1*b*. As the relative shear displacement between the indenter and the sample increases, the shear force increases to a peak value (stage 1). Beyond the peak, it decreases rapidly (stage 2) and then remains nearly constant (stage 3). Visual inspection of the contact region in stage 1 reveals that it changes in shape and size, but there is no macroscopic sliding between the indenter and the sample. In stage 3, the indenter slides steadily on the sample. More detailed explanations of the physics behind these different stages can be found in Shen *et al.* (2008). Briefly, in stage 1, the fibrils in contact with the indenter are loaded under shear. As shear increases, the elastic energy stored in these fibrils increases. This elastic energy is released suddenly in stage 2 due to the propagation of an interface crack. In stage 3, relative motion between the indenter and the sample appears to be accommodated by the propagation of Schallamach-like waves.

Owing to the applied shear displacement, the top of a typical fibril in a region enclosing the contact zone is displaced relative to the bottom. Figure 2 shows three optical micrographs of the contact region corresponding to the three points in figure 1*b*. In figure 2, the image of the top end of a fibril appears as a fuzzy grey circle, whereas the bottom end appears as a smaller dark square. This difference allows us to determine the relative deflection, Δ_T, of each fibril. The nearest-neighbour distance between fibrils is 87 µm, while their length is 67 µm. From figure 2*c*, it can be seen that the lateral displacement of a typical fibril can exceed its length. We show later that the usual small-deflection beam-column model (BCM; Timoshenko & Gere 1961) is not accurate enough to capture the deformation of microfibrils in our experiments. This motivates us to use a nonlinear large-deflection theory.

It should be noted that, when the same indentation test is performed on a flat unstructured control PDMS substrate, the contact area is found to decrease monotonically with increasing shear, consistent with a theory

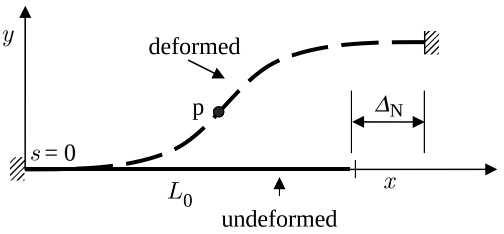

Figure 3. The coordinate system used in our analysis. The undeformed beam is straight and has length L_0. Both the ends of the beam are clamped. The right end is subjected to a vertical and tangential displacement Δ_N and Δ_T, respectively. The coordinates of the point 'p' are $(x(s), y(s))$.

proposed by Savkoor & Briggs (1977). In contrast, with increasing shear, the contact area for fibrillar samples initially increases. This difference in behaviour can be explained by the fact that, when a microfibril under shear bends, it significantly increases the normal compliance of the array. Since the normal load is fixed in these experiments, increase in normal compliance initially results in an increase in the contact area.

In order to develop a quantitative understanding of the load-bearing capacity of a fibrillar array under combined normal and shear loads, we study the nonlinear deformation of individual microfibrils. The model for fibril deflection and theoretical results based on it are presented in §2. In §3 we compare model predictions with the experiments.

2. ELASTICA MODEL OF A STRETCHABLE BEAM

We model the deformation of a typical microfibril in stage 1. Since the length of a typical microfibril is significantly greater than its lateral dimensions, it will be modelled as a stretchable elastica. Inside the contact zone, which is denoted by Ω_c, the thin film is well adhered to the indenter. Therefore, a fibril in Ω_c cannot rotate at this end, implying a clamped boundary condition. For a sufficiently long fibril, it is reasonable to assume that its bottom end is also clamped. We further assume that fibrils do not twist; this assumption is consistent with the loading conditions in our experiments. Finally, we neglect the compliance of the half-space to which the fibril is attached; this is again reasonable since fibrils are slender.

The problem of interest is an initially straight elastic beam with an initial length, L_0, that is clamped at both ends. One end of the beam is fixed to a rigid wall (the backing layer) while the other end is subjected to vertical and tangential displacements Δ_N and Δ_T, respectively. Let N_0, T_0, and M_0 denote the unknown normal, shear and moment applied at this end, respectively. Let s denote the arc length of the deformed beam and $x(s)$, $y(s)$ denote the deformed coordinates of the beam at a point 'p' on the bar (figure 3).

Following Frisch-Fay (1962), we assume a linear relation between curvature and moment, i.e.

$$EI\frac{d\psi}{ds} = M(s), \tag{2.1a}$$

where E is the Young modulus; I is the moment of inertia; ψ is the rotation of the deformed bar relative to the x-axis; and $M(s)$ is the moment acting at a generic point 'p'. (The free-body diagram of the bar is shown in figure 4.)

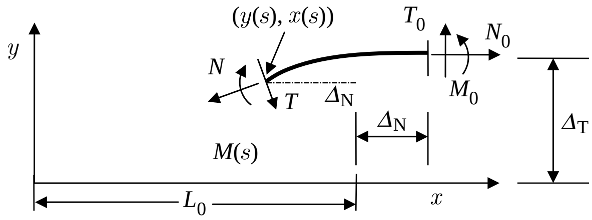

Figure 4. The free-body diagram of a section of the deformed bar. The right end of this section is clamped ($\psi=0$). Δ_T and Δ_N are the shear and normal displacements, respectively, at the right end of the beam. N_0 and T_0 denote the reaction forces, whereas the reaction moment is denoted by M_0.

The relevant boundary conditions are as follows:

$$\psi(s=0) = \psi(s=L) = 0, \tag{2.1b}$$

$$x(s=0) = 0 \qquad y(s=0) = 0, \tag{2.1c}$$

$$x(s=L) = L_0 + \Delta_N, \qquad y(s=L) = \Delta_T, \tag{2.1d}$$

where L denotes the deformed length of the beam. The free-body diagram in figure 4 shows that

$$M(s) = M_0 - N_0(\Delta_T - y(s)) + T_0(L_0 + \Delta_N - x(s)). \tag{2.2}$$

Substituting (2.2) into (2.1a) gives

$$\begin{aligned} EI\frac{d\psi}{ds} &= M(s) \\ &= M_0 - N_0(\Delta_T - y(s)) + T_0(L_0 + \Delta_N - x(s)). \end{aligned} \tag{2.3}$$

Let $N(s)$ and $T(s)$ denote the normal (normal to the cross section of the deformed bar) and shear forces along the deformed bar, respectively. Force balance requires that

$$\left.\begin{aligned} N\cos\psi - T\sin\psi &= N_0, \\ N\sin\psi + T\cos\psi &= T_0. \end{aligned}\right\} \tag{2.4}$$

Equation (2.4) implies that

$$N = N_0\cos\psi + T_0\sin\psi. \tag{2.5}$$

Note that, by definition,

$$\frac{dx}{ds} = \cos\psi, \tag{2.6a}$$

$$\frac{dy}{ds} = \sin\psi. \tag{2.6b}$$

Equations (2.6a) and (2.6b) imply that

$$x = \int_0^s \cos\psi(s')ds', \tag{2.7a}$$

$$y = \int_0^s \sin\psi(s')ds'. \tag{2.7b}$$

Combining (2.1d), (2.7a) and (2.7b), we have

$$L_0 + \Delta_N = \int_0^L \cos\psi(s')ds', \tag{2.8a}$$

$$\Delta_T = \int_0^L \sin\psi(s')ds'. \tag{2.8b}$$

To eliminate x and y from equation (2.3), we differentiate (2.3) by s and use (2.6a) and (2.6b),

$$EI\frac{d^2\psi}{ds^2} = N_0 \sin\psi(s) - T_0 \cos\psi(s). \tag{2.9}$$

Multiplying both sides of (2.9) by $d\psi/ds$ and integrating the resulting expression gives

$$\left(\frac{d\psi}{ds}\right)^2 = -\frac{2}{EI}(N_0 \cos\psi(s) + T_0 \sin\psi(s)) + D. \tag{2.10}$$

The integration constant D is determined using the boundary conditions $EI\, d\psi(s=L)/ds = M_0$ and $\psi(s=L)=0$, and is found to be

$$D = \frac{2}{EI}N_0 + \left[\frac{M_0}{EI}\right]^2. \tag{2.11}$$

Integrating (2.10) with respect to ψ, we obtain

$$s = \int_0^{\psi} \frac{d\psi'}{\sqrt{-\frac{2}{EI}(N_0 \cos\psi' + T_0 \sin\psi') + D}}, \quad 0 \le \psi \le \psi_{\max}, \tag{2.12}$$

where we have retained only the positive root. By symmetry (figure 3), the angle ψ increases with arc length, s, from either end and reaches a maximum value of $\psi_{\max}$ at the midpoint. The value of $\psi_{\max}$ is found using $d\psi/ds=0$,

$$-\frac{2}{EI}(N_0 \cos\psi_{\max} + T_0 \sin\psi_{\max}) + D = 0. \tag{2.13}$$

2.1. *Extensibility*

Let λ denote the stretch ratio of a material point 'p' on the beam. It can be labelled by its coordinates, X, on the initially straight beam, which coincides with the horizontal axis, i.e. $X \in (0, L_0)$. Point 'p' is displaced to coordinates $(x(s),\ y(s))$ on the deformed beam. Assuming that the stretch is proportional to the local normal force,

$$\lambda = \frac{ds}{dX} \Leftrightarrow \lambda - 1 = \frac{ds - dX}{dX} = cN(x(s),\ y(s)) \Leftrightarrow \frac{ds}{dX} = 1 + cN(x(s),\ y(s)), \tag{2.14}$$

where $c=1/EA$ and A is the cross-sectional area of the beam. Equation (2.14) can be integrated to give

$$\int_0^L \frac{ds'}{1 + cN(x(s'),\ y(s'))} = \int_0^{L_0} dX = L_0. \tag{2.15}$$

Using (2.5), equation (2.15) becomes

$$\int_0^L \frac{ds'}{1 + c[N_0 \cos\psi(s') + T_0 \sin\psi(s')]} = L_0. \tag{2.16}$$

For a given T_0 and N_0, one can solve equations (2.8a), (2.8b), (2.12) and (2.16) for Δ_N, Δ_T, M_0 and L, with

$$\psi\left(s = \frac{L}{2}\right) = \psi_{\max}. \tag{2.17}$$

2.2. *An equivalent problem*

The deflection in figure 3 can also be obtained by moving the right (left) end of the beam up (down) by $\pm\Delta_T/2$ and outwards by $\Delta_N/2$, with the midpoint of the beam fixed. If we measure s from the left end of the beam, then it is easily seen that $\psi_{\max}$ is attained at $s=L/2$. In addition, we can solve the problem for $s\in(0,\ L/2)$. The boundary conditions are

$$\psi(s=0) = 0, \tag{2.18a}$$

$$\psi'(s=L/2) = 0, \tag{2.18b}$$

$$\psi\left(s = \frac{L}{2}\right) = \psi_{\max}, \tag{2.18c}$$

$$x(s=0) = y(s=0) = 0, \tag{2.18d}$$

$$x(s=L/2) = (L_0 + \Delta_N)/2, \tag{2.18e}$$

$$y(s=L/2) = \Delta_T/2. \tag{2.18f}$$

The known quantities are N_0, T_0, L_0; the unknowns are Δ_N, Δ_T, L and the constant D. The constant D can be expressed in terms of the unknowns Δ_N, Δ_T, using (2.11) and noting that the moment at the centre of the deflected beam is zero, i.e.

$$M_0 + \frac{(L_0 + \Delta_N)T_0}{2} - N_0\frac{\Delta_T}{2} = 0. \tag{2.19}$$

The extensibility condition, equation (2.16), becomes

$$\int_0^{L/2} \frac{ds'}{1 + c[N_0 \cos\psi(s') + T_0 \sin\psi(s')]} = L_0/2. \tag{2.20}$$

Likewise, equations (2.8a) and (2.8b) become

$$\frac{L_0 + \Delta_N}{2} = \int_0^{L/2} \cos\psi(s')ds', \tag{2.21a}$$

$$\frac{\Delta_T}{2} = \int_0^{L/2} \sin\psi(s')ds'. \tag{2.21b}$$

Given N_0, T_0, L_0, equations (2.12), (2.20), (2.21a) and (2.21b) can be solved to find the unknowns Δ_N, Δ_T, L.

2.3. *Results*

There is a simple way to solve the above problem and to reduce the solution to elliptic integrals (see equations (A 20), (A 22) and (A 23b) in appendix A). Details are given in appendix A; here we state the main results.

The problem can be reduced to the solution of the following three decoupled equations:

$$\sqrt{\frac{EI}{2\Lambda}}\int_{\theta_0}^{q_{\max}} \frac{dq}{(1 + c\Lambda \sin q)\sqrt{\sin q_{\max} - \sin q}} = L_0/2, \tag{2.22}$$

$$\frac{\Delta_T}{2} = \sqrt{\frac{EI}{2\Lambda}}\int_{\theta_0}^{q_{\max}} \sin(q - \theta_0)\frac{dq}{\sqrt{\sin q_{\max} - \sin q}}, \tag{2.23}$$

$$\frac{(L_0 + \Delta_N)}{2} = \sqrt{\frac{EI}{2\Lambda}}\int_{\theta_0}^{q_{\max}} \cos(q - \theta_0)\frac{dq}{\sqrt{\sin q_{\max} - \sin q}}, \tag{2.24}$$

where Λ is the magnitude of the total applied force, i.e.

$$\Lambda = \sqrt{N_0^2 + T_0^2} \tag{2.25a}$$

and θ_0 is the phase angle of the applied force, i.e.

$$N_0/\Lambda = \sin\theta_0, \qquad T_0/\Lambda = \cos\theta_0. \tag{2.25b}$$

Finally,

$$q_{\max} \equiv \theta_0 + \psi_{\max}, \tag{2.26}$$

in (2.22)–(2.24). To find Δ_{N} and Δ_{T} given T_0 and N_0, we solve equation (2.22) for $q_{\max}$ given T_0 and N_0. We then substitute $q_{\max}$ into (2.23) and (2.24) to find Δ_{N} and Δ_{T}.

2.4. Normalization

To expedite the analysis, we define the following normalized variables:

$$\left.\begin{aligned} \bar{T}_0 &= \frac{T_0 L_0^2}{2EI}, \\ \bar{N}_0 = \frac{N_0 L_0^2}{2EI} \quad \bar{\Lambda} &= \frac{\Lambda L_0^2}{2EI} \quad \bar{\Delta}_{\mathrm{T,N}} = \Delta_{\mathrm{T,N}}/L_0. \end{aligned}\right\} \tag{2.27}$$

After normalization, equations (2.22)–(2.24) become

$$\int_{\theta_0}^{q_{\max}} \frac{\mathrm{d}q}{\left(1 + c\frac{2EI}{L_0^2}\bar{\Lambda}\sin q\right)\sqrt{\sin q_{\max} - \sin q}} = \sqrt{\bar{\Lambda}}, \tag{2.28}$$

$$\bar{\Delta}_{\mathrm{T}} = \frac{1}{\sqrt{\bar{\Lambda}}}\int_{\theta_0}^{q_{\max}} \frac{\sin(q-\theta_0)}{\sqrt{\sin q_{\max} - \sin q}}\,\mathrm{d}q, \tag{2.29}$$

$$1 + \bar{\Delta}_{\mathrm{N}} = \frac{1}{\sqrt{\bar{\Lambda}}}\int_{\theta_0}^{q_{\max}} \cos(q-\theta_0)\frac{\mathrm{d}q}{\sqrt{\sin q_{\max} - \sin q}}. \tag{2.30}$$

It is interesting to note that the normalized equations (2.28)–(2.30) depend on two dimensionless parameters: θ_0, which is the phase angle of loading, and $2cEI/L_0^2 = 2I/AL_0^2$, which is a purely geometric quantity. For a beam with a square cross section with side length b, $2I/AL_0^2$ is proportional to $(b/L_0)^2$, the aspect ratio squared. The numerical results presented in §2.5 are for $b=14$ μm and length $L_0=67$ μm, which are the dimensions of fibrils used in our experiments.

2.5. Numerical results

The normalized shear displacement $\bar{\Delta}_{\mathrm{T}}$ is plotted against $\bar{T}_0$ for $\bar{N}_0 = 0$ in figure 5. The prediction of the BCM (derived in appendix B for our boundary condition) for small $\bar{\Lambda}$ is

$$\bar{\Delta}_{\mathrm{T}} = \frac{1}{6}\bar{T}_0, \tag{2.31}$$

$$\bar{\Delta}_{\mathrm{N}} = \bar{C}_{\mathrm{N0}}\bar{N}_0 + \frac{1}{6}\frac{\bar{C}_{\mathrm{N0}}}{(1-\bar{C}_{\mathrm{N0}}\bar{N}_0)}\bar{T}_0^2, \tag{2.32}$$

where $\bar{C}_{\mathrm{N0}} \equiv 2I/b^2L_0^2$ is the normalized compliance for a bar under a pure normal load. Note that the shear compliance for small $\bar{\Lambda}$ is independent of the normal load.

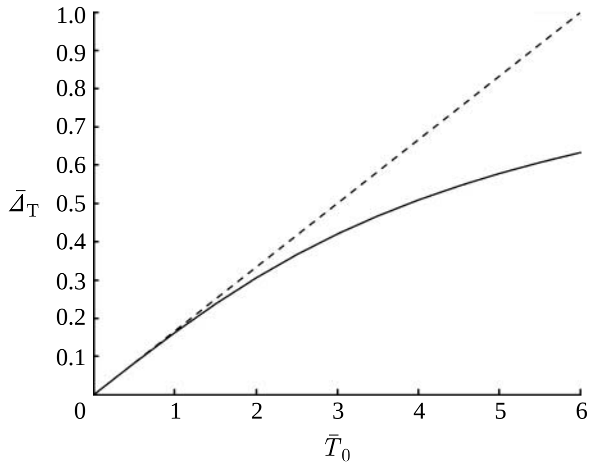

Figure 5. Normalized shear displacement, $\bar{\Delta}_{\mathrm{T}}$, versus normalized shear force, $\bar{T}_0$, for $\bar{N}_0=0$ (or $\theta_0=0$) and $b/L_0=14/67$. Solid line, the solution of the nonlinear theory (2.28)–(2.30); dashed line, the prediction of BCM (2.31).

Figure 5 shows that the small-deflection BCM result (equations (2.31) and (2.32)) for $\bar{N}_0=0$ is accurate as long as $\bar{T}_0 \le 1.5$ or when the shear displacement is less than 30% of the original length of the beam.

Figure 6 plots the normalized shear displacement $\bar{\Delta}_{\mathrm{T}}$ versus the normalized shear load $\bar{T}_0$ for different normalized normal forces $\bar{N}_0$ or θ_0. The normalized compressive load in figure 6 is chosen to be less than the buckling load. Owing to adhesion, a fibril (e.g. those at the edge of the contact zone) can be subjected to tension (i.e. $N_0>0$). The incremental shear compliance at a fixed normal load is $\partial\bar{\Delta}_{\mathrm{T}}/\partial\bar{T}_0$. The prediction of the BCM is indicated by the dashed line. In the BCM, the shear compliance is independent of the normal load (see appendix B). Figure 6 shows that the BCM is valid only in the limit when both normal and shear forces are small. For example, even for small deflections, the shear compliance is not a constant but increases with increasing compression (more negative $\bar{N}_0$). In general, when the beam is under compression, the BCM theory underestimates the shear compliance for small shear and it overestimates it for large shear. It is also clear from figure 6*a* that, for the range of deflections of interest in our experiments ($\bar{\Delta}_{\mathrm{T}} \approx 1$), the shear force predicted by the small-deflection theory can be much smaller than that predicted by the nonlinear theory. The normalized incremental shear compliance $\bar{C}_{\mathrm{T}} = \partial\bar{\Delta}_{\mathrm{T}}/\partial\bar{T}_0|_{N_0=0}$ versus Δ_{T} for different three normal forces is shown in figure 6*b*. The dashed line is the prediction of the BCM. Note that, for $\bar{\Delta}_{\mathrm{T}} \ge 0.75$, the incremental shear compliance for different normal loads becomes nearly identical. In this regime, the shear response is governed almost entirely by stretching of the fibril.

Figure 7 shows that a fibril with no applied normal load can still have normal displacement due to shear. Figure 7 also shows that the small-deflection theory considerably underestimates the normal displacement for large $\bar{T}_0$. To study the incremental normal compliance of the fibril $\bar{C}_{\mathrm{N}} = \partial\bar{\Delta}_{\mathrm{N}}/\partial\bar{N}_0|_{\bar{T}_0}$, the dependence of $\bar{\Delta}_{\mathrm{N}}$ on $\bar{N}_0$ for different $\bar{T}_0$ is shown in figure 8*a*. For small $\bar{T}_0$, the compliance is small. For a fixed $\bar{N}_0$, the incremental normal compliance increases

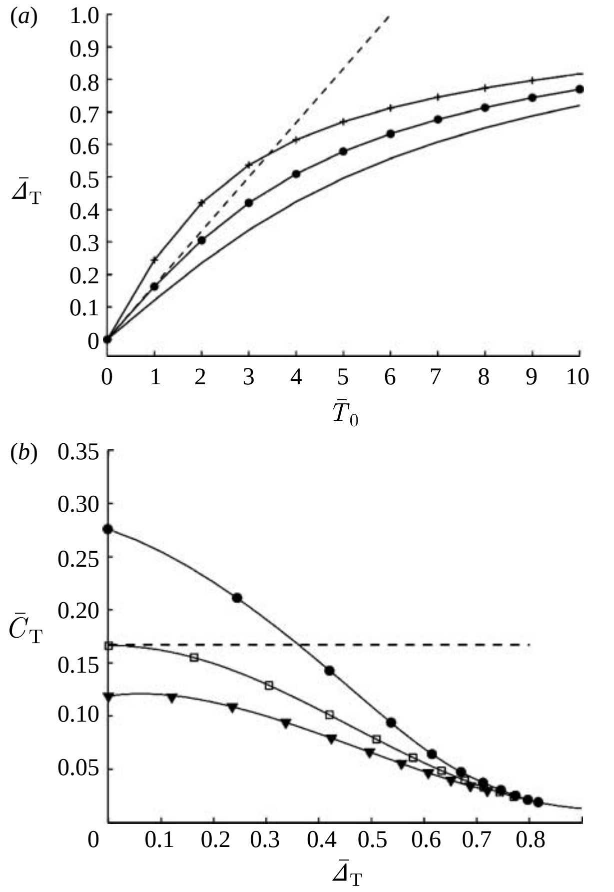

Figure 6. (*a*) The normalized shear displacement versus shear force for different applied normal loads. The dashed line is the BCM (2.31) for $\bar{N}_0=0$ (circles, $\bar{N}_0=0$; crosses, $\bar{N}_0=-2$; solid line, $\bar{N}_0=2$). (*b*) The incremental shear compliance versus normalized shear displacement for different applied normal loads. The dashed line is the BCM (2.31) for $\bar{N}_0=0$ (squares, $\bar{N}_0=0$; filled circles, $\bar{N}_0=-2$; inverted triangles, $\bar{N}_0=2$). The symbols are the numerical solution of (2.28)–(2.30).

significantly with increasing applied shear load $\bar{T}_0$; for a fixed $\bar{T}_0$, it also increases slightly with increasing compressive normal load, as shown in figure 8*b*.

3. COMPARISON WITH THE EXPERIMENTS

We give an example to illustrate how our model can be used to interpret the experiments. As mentioned in §1, the relative deflection of the fibrils (i.e. Δ_T's) can be measured in our experiments. Since fibrils far away from the contact zone Ω_c do not carry load, we need only to measure deflections inside a sufficiently large region Ω that contains Ω_c. In our experiments, the normal force applied on the indenter, F_N, is much smaller than the typical shear force F_s on the sphere. Therefore, we assume that the normal force N_0 acting on each fibril is approximately zero. With this assumption, Δ_T and N_0 are known for each fibril ($N_0=0$), and the shear force, T_0, acting on these fibrils can be computed using our model. To expedite the computation, the result of figure 9 is represented as a relationship between $\bar{T}_0$ and $\bar{\Delta}_T$ using a seventh-degree polynomial, i.e.

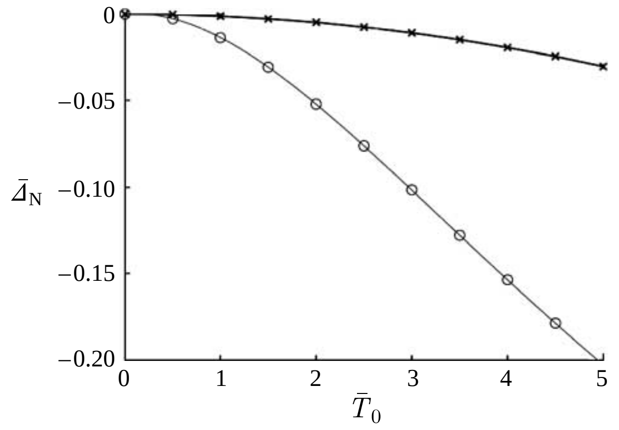

Figure 7. The normalized normal displacement, $\bar{\Delta}_N$, versus normalized shear force $\bar{T}_0$, for $\bar{N}_0=0$ (or $\theta_0=0$). It shows that a significant normal deflection at the fibril end can occur with no applied normal force. Note that the small-deflection theory underestimates the normal displacement. Circles, large-deflection theory; crosses, small-deflection BCM.

$$\bar{T}_0=261.65\bar{\Delta}_T^7-1296.2\bar{\Delta}_T^6+2373.5\bar{\Delta}_T^5-1950.9\bar{\Delta}_T^4+765.36\bar{\Delta}_T^3-117\bar{\Delta}_T^2+6\bar{\Delta}_T. \quad (3.1)$$

Figure 9 shows that equation (3.1) is very accurate and converges to (2.31) for very small $\bar{\Delta}_T$.

The total shear force acting on the indenter, F_s, is given by

$$F_s=\sum_{i=1}^{n} T_0(i), \quad (3.2)$$

where $T_0(i)$ denotes the shear force acting on the *i*th fibril and n is the total number of fibrils in Ω. It should be noted that, while fibrils inside Ω_c obey the clamped–clamped boundary condition, the top of the fibrils in $\Omega-\Omega_c$ can rotate freely. However, there is no difficulty in computing T_0 for these fibrils. Indeed, the deformation of these fibrils can be obtained by replacing $L_0/2$ in (2.22) by L_0, $\Delta_T/2$ in (2.23) by Δ_T and $(L_0+\Delta_N)/2$ in (2.24) by $L_0+\Delta_N$.

We obtain $T_0(i)$ using the following procedure. First, we select three points on the shear force versus shear displacement curve in figure 1*b*. The coordinates of these points are A(0.0155 mm, 3.80 mN), B(0.0456 mm, 18.68 mN) and C(0.106 mm, 40.03 mN), respectively. We select Ω with the condition that fibrils outside of Ω do not have measurable deflections. Once this is done, we measure the deflection for each fibril ($\Delta_T(i)$) inside Ω. $\bar{\Delta}_T(i)$ in (3.1) is computed from $\Delta_T(i)$ using $L=67$ μm. We then use (3.1) to obtain $\bar{T}_0(i)$. To compute $T_0(i)$ from $\bar{T}_0(i)$, we need the Young modulus and the moment of inertia I. We use a Young modulus of 3 MPa for PDMS, the fibril material. This modulus has been measured independently using an indentation test (see Noderer *et al.* 2007). The moment of inertia I is 3.2×10^3 (μm)^4 since the fibrils in our experiments have a square cross section of 14 μm. The number of fibrils in Ω is 324. We then compute the indenter shear forces using

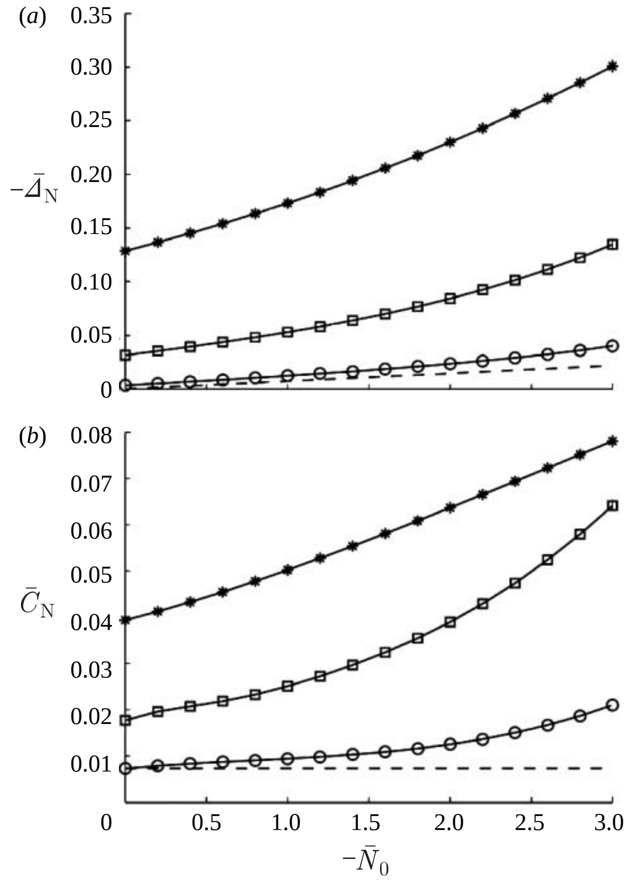

Figure 8. (*a*) The dependence of $\bar{\Delta}_N$ on $\bar{N}_0$ for different $\bar{T}_0$. (*b*) The normalized normal compliance of a fibril against $\bar{N}_0$ for different $\bar{T}_0$. It shows that, for small $\bar{T}_0$, the incremental compliance is small. For a fixed $\bar{N}_0$, the incremental normal compliance increases significantly with increasing applied shear load $\bar{T}_0$; for a fixed $\bar{T}_0$, it also increases slightly with increasing normal load. The dashed lines are the predictions of the BCM with $\bar{T}_0 = 0$. Circles, $\bar{T}_0 = 0.5$; squares, $\bar{T}_0 = 1.5$; asterisks, $\bar{T}_0 = 3.5$.

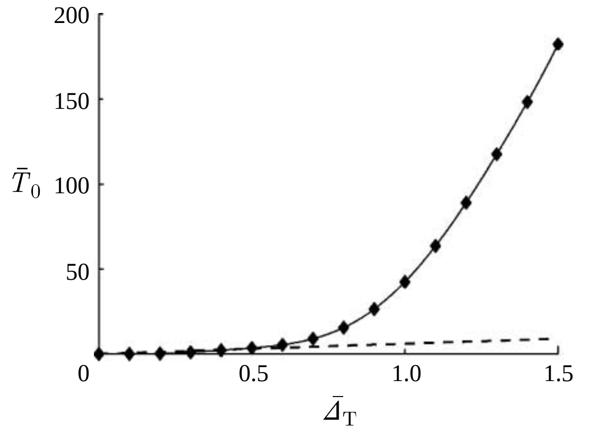

Figure 9. Normalized shear force versus normalized shear displacement for $N_0 = 0$. The dashed line is the small-deflection BCM (2.31). The seventh-order polynomial fit (3.1) (solid line) captures the numerical result (diamonds) obtained by solving (2.28)–(2.30). Normal compression is assumed to be zero.

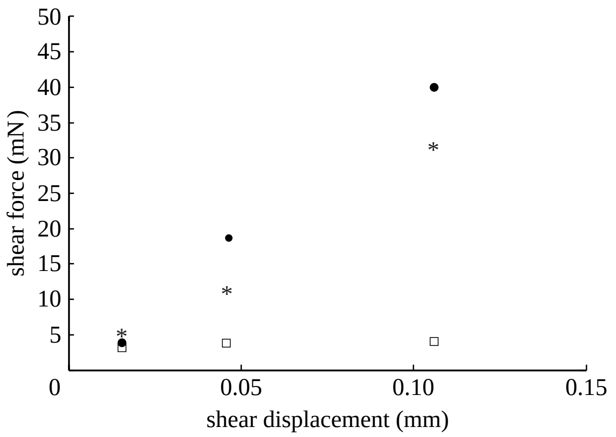

Figure 10. Comparison of the experimental data (stage 1, filled circles) with the large (asterisks) and small (squares) deflection theoretical results. The small-deflection theory (BCM) works well for very small shear displacements but considerably underestimates the shear force for large shear displacements.

(3.2). They are 5.23 mN for point A, 11.22 mN for point B and 31.54 mN for point C. We also use the small-deflection theory (2.31) to compute these shear forces. They are 3.24 mN for point A, 3.75 mN for point B and 4.02 mN for point C. These results are shown in figure 10, which compares the experimental data (stage 1) with the large- and small-deflection results. As expected, the small-deflection theory works well for small shear displacements but strongly underestimates the shear force for large shear displacements. For example, near the peak load (e.g. point C), the use of the small-deflection theory underestimates the shear force by approximately an order of magnitude. Given the fact that we have used no adjustable parameters, the agreement between our large-deflection theory and the experimental data is quite good.

4. DISCUSSION AND CONCLUSION

The mechanical behaviour of fibrils under combined normal and shear loads underlies the response of biomimetic fibrillar arrays. Deformations are typically large compared with fibril dimensions. We have developed a nonlinear model to compute the deflection of fibrils in microfibril arrays subjected to normal and shear loads. To simplify the analysis, we have assumed that the fibrils do not twist. Also, we assume that the beam can undergo very large deflection but material behaviour is still linear.

Our model isolates a single fibril in the array to study its behaviour, whereas, in practice, the entire array is subjected to normal and shear loads. To illustrate how our model can be applied in this situation, we use our model to predict the shear force acting on a glass indenter in contact with an array of film-terminated fibrils. The computed shear forces are then compared with those obtained from the experiments. In the simulations, we have made the approximation that the normal force acting on all the fibrils is zero, which is strictly valid only for fibrils that are outside the contact zone. For fibrils inside the contact zone, some of the fibrils can be under tension (e.g. those close to the contact edge), whereas others can be under compression, hence our assumption is only approximately valid if the normal indentation force is very small in comparison with the shear forces, which is the case in our experiments. Nevertheless, the prediction of our nonlinear model is in reasonably good agreement with the experimental data. We should point out that there is some error in measuring the relative displacement of each fibril. Since the nonlinear theory is very sensitive to the relative shear displacement, it is not surprising that the nonlinear theory did worst for small deflections, where the relative error of the measurements can be large. Finally, there is no fitting parameter in our calculation.

Although our analysis is valid for any loading phase angle as well as for arbitrary aspect ratios, explicit results are presented for a particular aspect ratio. Also, we focus on the case where the normal load is zero. In general, there is no difficulty in generating results for other aspect ratios and different phase angles. Also, our model can be easily modified to describe the deformation of preoriented fibrils.

The model of fibril deformation studied in this work is quite general and can be used to study fibrillar structures other than our own. For example, it is applicable to a similar fibrillar structure (with angled fibrils) fabricated recently by Yao *et al.* (2007). It can also be used to analyse the shear deformation of fibrils with spatulated tips, such as those fabricated by Kim *et al.* (2007).

The analysis will be more complicated for the general case where the normal indentation force is significant. In this case, most of the fibrils inside the contact zone will be under compression except those near the edge. These edge fibrils will be under tension owing to adhesion. For this case, the normal and shear loads on each fibril in the array must be determined using the contact condition. This will be studied in a future work.

This work was supported by a grant from the Department of Energy under award number DE-FG02-07ER46463.

APPENDIX A. DERIVATION OF (2.22)–(2.24)

Substituting (2.13) into (2.12) gives

$$s=\int_0^{\psi}\frac{\mathrm{d}\psi'}{\sqrt{\begin{array}{l}\frac{2}{EI}(N_0\cos\psi_{\max}+T_0\sin\psi_{\max})\\ -\frac{2}{EI}(N_0\cos\psi'+T_0\sin\psi')\end{array}}}. \tag{A 1}$$

Using (2.25*a*) and (2.25*b*), the terms inside the square root in (A 1) are

$$\frac{2}{EI}(N_0\cos\psi_{\max}+T_0\sin\psi_{\max})$$
$$-\frac{2}{EI}(N_0\cos\psi'+T_0\sin\psi')=\frac{2\Lambda}{EI}(\sin q_{\max}-\sin q), \tag{A 2}$$

where

$$q\equiv(\theta_0+\psi'),\qquad q_{\max}\equiv(\theta_0+\psi_{\max}). \tag{A 3}$$

Since

$$\frac{2\Lambda}{EI}(\sin q_{\max}-\sin q)=\frac{2\Lambda}{EI}(1+\sin q_{\max}-1-\sin q), \tag{A 4}$$

we can define a constant p by

$$2p^2\equiv 1+\sin q_{\max}=1+\sin(\theta_0+\psi_{\max}). \tag{A 5}$$

Note that $0\le p\le 1$. Also, introduce a new variable ϕ by

$$1+\sin q\equiv 2p^2\sin^2\phi, \tag{A 6}$$

so that (A 4) is

$$\sqrt{\frac{2\Lambda}{EI}(\sin q_{\max}-\sin q)}=2\sqrt{\frac{\Lambda}{EI}}p\cos\phi. \tag{A 7}$$

It is easy to verify that

$$\mathrm{d}\psi'=\mathrm{d}q=\frac{2p\cos\phi\,\mathrm{d}\phi}{\sqrt{1-p^2\sin^2\phi}}. \tag{A 8}$$

Substituting (A 7) and (A 8) into (A 1), we have

$$s=\sqrt{\frac{EI}{\Lambda}}\int_{\phi_0}^{\phi}\frac{\mathrm{d}\phi'}{\sqrt{1-p^2\sin^2\phi'}}, \tag{A 9}$$

where

$$\phi_0=\sin^{-1}\left[\sqrt{\frac{1+\sin\theta_0}{2p^2}}\right]. \tag{A 10}$$

Equations (A 5) and (A 6) imply that

$$\psi=\psi_{\max}\Leftrightarrow q=q_{\max}\Leftrightarrow\phi=\frac{\pi}{2}. \tag{A 11}$$

Thus, setting $\phi=\pi/2$ in (A 9) gives

$$L/2=\sqrt{\frac{EI}{\Lambda}}\int_{\phi_0}^{\pi/2}\frac{\mathrm{d}\phi'}{\sqrt{1-p^2\sin^2\phi'}}. \tag{A 12}$$

Equations (A 3) and (A 9) imply that

$$\begin{aligned}\mathrm{d}s&=\sqrt{\frac{EI}{2\Lambda}}\frac{\mathrm{d}\psi}{\sqrt{(\sin q_{\max}-\sin q)}}\\&=\sqrt{\frac{EI}{2\Lambda}}\frac{\mathrm{d}q}{\sqrt{(\sin q_{\max}-\sin q)}},\end{aligned} \tag{A 13}$$

so (2.21*a*) is

$$\frac{(L_0+\Delta_{\mathrm{N}})}{2}=\sqrt{\frac{EI}{2\Lambda}}\int_{\theta_0}^{\theta_0+\psi_{\max}}\frac{\cos(q-\theta_0)\mathrm{d}q}{\sqrt{(\sin q_{\max}-\sin q)}}, \tag{A 14}$$

which is (2.24). Equation (A 14) can be rewritten as

$$\frac{(L_0+\Delta_{\mathrm{N}})}{2}=\sqrt{\frac{EI}{2\Lambda}}\left[\cos\theta_0\int_{\theta_0}^{\theta_0+\psi_{\max}}\frac{\cos q\,\mathrm{d}q}{\sqrt{(\sin q_{\max}-\sin q)}}+\sin\theta_0\int_{\theta_0}^{\theta_0+\psi_{\max}}\frac{\sin q\,\mathrm{d}q}{\sqrt{(\sin q_{\max}-\sin q)}}\right]. \tag{A 15}$$

The first integral in (A 15) can be integrated exactly, i.e.

$$\int_{\theta_0}^{\theta_0+\psi_{\max}}\frac{\cos q\,\mathrm{d}q}{\sqrt{(\sin q_{\max}-\sin q)}}=2\sqrt{\sin(\theta_0+\psi_{\max})-\sin\theta_0}. \tag{A 16}$$

The second integral can be expressed in terms of elliptic functions using (A 5)–(A 7)

$$\int_{\theta_0}^{\theta_0+\psi_{\max}} \frac{\sin q\,\mathrm{d}q}{\sqrt{(\sin q_{\max}-\sin q)}}$$
$$=\sqrt{2}[-2E(p)+2E(\phi_0,p)+K(p)-F(\phi_0,p)], \quad (\text{A }17)$$

where

$$F(\phi_0,p)\equiv\int_0^{\phi_0}\frac{1}{\sqrt{1-p^2\sin^2\phi}}\,\mathrm{d}\phi \quad (\text{A }18)$$

is the incomplete elliptic integral of the first kind; $K(p)=F(\pi/2,p)$ is the complete elliptic integral of the first kind;

$$E(\phi_0,p)=\int_0^{\phi_0}\sqrt{1-p^2\sin^2\phi}\,\mathrm{d}\phi \quad (\text{A }19)$$

is the incomplete elliptic integral of the second kind; and $E(p)=E(\pi/2,p)$ is the complete elliptic integral of the second kind. Using (A 16) and (A 17), (A 14) becomes

$$\frac{(L_0+\Delta_{\mathrm{N}})}{2}=\sqrt{\frac{EI}{\Lambda}}\Big[\sqrt{2}\cos\theta_0\sqrt{\sin(\theta_0+\psi_{\max})-\sin\theta_0}$$
$$+\sin\theta_0[-2E(p)+2E(p,\phi_0)+K(p)-F(p,\phi_0)]\Big]. \quad (\text{A }20)$$

Likewise, (2.23) can be obtained by substituting (A 13) into (2.21*b*),

$$\Delta_{\mathrm{T}}/2=\int_0^{L/2}\sin\psi(s')\mathrm{d}s'$$
$$=\sqrt{\frac{EI}{2\Lambda}}\int_{\theta_0}^{q_{\max}}\sin(q-\theta_0)\frac{\mathrm{d}q}{\sqrt{\sin q_{\max}-\sin q}}. \quad (\text{A }21)$$

In exactly the same way, (A 21) becomes

$$\Delta_{\mathrm{T}}/2=\sqrt{\frac{EI}{\Lambda}}\Big[-\sqrt{2}\sin\theta_0\sqrt{\sin(\theta_0+\psi_{\max})-\sin\theta_0}$$
$$+\cos\theta_0[-2E(p)+2E(p,\phi_0)+K(p)-F(p,\phi_0)]\Big]. \quad (\text{A }22)$$

Using (A 2) and (A 13), (2.20) becomes

$$\sqrt{\frac{EI}{2\Lambda}}\int_{\theta_0}^{q_{\max}}\frac{\mathrm{d}q}{(1+c\Lambda\sin q)\sqrt{\sin q_{\max}-\sin q}}=L_0/2. \quad (\text{A }23a)$$

Equation (A 23*a*) can be expressed in terms of incomplete elliptic integral of the third kind, $\Pi(n;\phi,k)$, i.e.

$$-\frac{1}{(1+c\Lambda\sin q_{\max})\sqrt{1+\sin q_{\max}}}$$
$$\Pi\left(\sqrt{\frac{\sin\theta_0-\sin q_{\max}}{1-\sin q_{\max}}};\frac{(\sin q_{\max}-1)c\Lambda}{1+c\Lambda\sin q_{\max}},\mathrm{i}\frac{|\cos q_{\max}|}{1+\sin q_{\max}}\right)$$
$$=\frac{1}{2}\sqrt{\frac{\Lambda L_0^2}{2EI}}, \quad (\text{A}23b)$$

where

$$\Pi(n;\phi,k)=\int_0^{\phi}\frac{\mathrm{d}\theta}{(1-n\sin^2\theta)\sqrt{1-k^2\sin^2\theta}}. \quad (\text{A }24)$$

APPENDIX B. SMALL-ANGLE APPROXIMATION (SMALL-DEFLECTION APPROXIMATION)

Assuming ψ is small, (2.10) can be approximated at

$$\frac{\mathrm{d}\psi}{\mathrm{d}s}\approx\sqrt{-\frac{2}{EI}(N_0+T_0\psi(s))+D}, \quad 0<s<L/2. \quad (\text{B }1)$$

Substituting $D=2/EI(N_0\cos\psi_{\max}+T_0\sin\psi_{\max})\approx 2/EI(N_0+T_0\psi_{\max})$ into (B 1) and integrating, we have

$$s\approx\sqrt{\frac{EI}{2T_0}}\int_0^{\psi}\frac{\mathrm{d}\psi'}{\sqrt{\psi_{\max}-\psi'}}$$
$$=\sqrt{\frac{2EI}{T_0}}\Big[\sqrt{\psi_{\max}}-\sqrt{\psi_{\max}-\psi}\Big], \quad \psi_{\max}>\psi, \quad (\text{B }2)$$

or

$$\psi=\psi_{\max}-\left[\sqrt{\frac{T_0}{2EI}}s-\sqrt{\psi_{\max}}\right]^2. \quad (\text{B }3)$$

Using (2.10) and (2.11) and the fact that $(\mathrm{d}\psi/\mathrm{d}s)=0$ at $\psi=\psi_{\max}$, we have

$$-\frac{2}{EI}(N_0+T_0\psi_{\max})+D=0$$
$$\Leftrightarrow-\frac{2}{EI}T_0\psi_{\max}+\left[\frac{M_0}{EI}\right]^2=0\Rightarrow\psi_{\max}=\frac{1}{2T_0}\left[\frac{M_0^2}{EI}\right]. \quad (\text{B }4)$$

Since $\psi=\psi_{\max}$ when $s=L/2$, (B 3) implies that

$$\psi_{\max}=\frac{T_0L^2}{8EI}. \quad (\text{B }5)$$

Using (B 4), we have

$$M_0=-\frac{T_0L}{2}. \quad (\text{B }6)$$

Combining (B 3) and (B 5) gives

$$\psi=\frac{T_0}{2EI}s(L-s). \quad (\text{B }7)$$

Using (B 5), the small-deflection version of (2.21*b*) is

$$\Delta_{\mathrm{T}}/2\approx\int_0^{L/2}\psi(s')\mathrm{d}s'=\frac{T_0L^3}{24EI}. \quad (\text{B }8)$$

The normalized form of (B 8) is (2.31) using $L\approx L_0$,

$$\bar{\Delta}_{\mathrm{T}}=\frac{1}{6}\bar{T}_0. \quad (\text{B }9)$$

To determine the relationship between normal displacement and normal load for small deflections, we approximate (2.20) by assuming that the slope is small, so that $\psi\approx y'$, $\mathrm{d}s\approx\mathrm{d}x$, i.e.

$$\int_0^{L/2}\frac{\mathrm{d}x}{1+c[N_0+T_0y']}=L_0/2. \quad (\text{B }10)$$

Consistent with small deflections, we assume

$$cT_0y'/(1+cN_0)\ll 1. \quad (\text{B }11)$$

The integral in (B 10) can be written as

$$\int_0^{L/2} \frac{\mathrm{d}x}{(1+cN_0)\left[1+\frac{cT_0 y'}{(1+cN_0)}\right]} \approx \frac{1}{(1+cN_0)}$$

$$\int_0^{L/2}\left[1-\frac{cT_0 y'}{(1+cN_0)}\right]\mathrm{d}x = \frac{1}{(1+cN_0)}\left[\frac{L}{2}-\frac{cT_0 \Delta_T}{2(1+cN_0)}\right], \tag{B 12}$$

where we have used

$$\int_0^{L/2} y'\,\mathrm{d}x = y(L/2) = \Delta_\mathrm{T}/2. \tag{B 13}$$

Using (B 12) and (B 13), (B 10) becomes

$$\Delta_n - \frac{cT_0\Delta_\mathrm{T}}{(1+cN_0)} = L_0 cN_0, \tag{B 14}$$

where $L \approx L_0 + \Delta_\mathrm{N}$. Equation (2.32) is obtained by substituting (B 9) into (B 14), i.e.

$$\Delta_n = L_0 cN_0 + \frac{12cEI\Delta_\mathrm{T}^2}{L^3(1+cN_0)}. \tag{B 15}$$

REFERENCES

Aksak, B., Murphy, M. P. & Sitti, M. 2007 Adhesion of biologically inspired vertical and angled polymer microfiber arrays. *Langmuir* **23**, 3322–3332. (doi:10.1021/la062697t)

Autumn, K., Liang, Y. A., Hsieh, S. T., Zesch, W., Chan, W. P., Kenny, T. W., Fearing, R. & Full, R. J. 2000 Adhesive force of a single gecko foot-hair. *Nature* **405**, 681–685. (doi:10.1038/35015073)

Bhushan, B., Peressadko, A. G. & Kim, T. W. 2006 Adhesion analysis of two-level hierarchical morphology in natural attachment systems for 'smart adhesion'. *J. Adhes. Sci. Technol.* **20**, 1475–1491. (doi:10.1163/156856106778666408)

Chen, S. & Gao, H. 2007 Non-slipping adhesive contact between mismatched elastic spheres: a model of adhesion mediated deformation sensor. *J. Mech. Phys. Solids* **55**, 1001–1015. (doi:10.1016/j.jmps.2006.10.008)

Chung, J. Y. & Chaudhury, M. K. 2005 Roles of discontinuities in bio-inspired adhesive pads. *J. R. Soc. Interface* **2**, 55–61. (doi:10.1098/rsif.2004.0020)

Crosby, A. J., Hageman, M. & Duncan, A. 2005 Controlling polymer adhesion with 'pancakes'. *Langmuir* **21**, 11 738–11 743. (doi:10.1021/la051721k)

Frisch-Fay, R. 1962 *Flexible bars*, pp. 33–44. Washington, DC: Butterworths.

Gao, H., Ji, B., Jäger, I. L., Arzt, E. & Fratzl, P. 2003 Materials become insensitive to flaws at nanoscale: lessons from nature. *Proc. Natl Acad. Sci. USA* **100**, 5597–5600. (doi:10.1073/pnas.0631609100)

Gao, H., Wang, X., Yao, H., Gorb, S. & Arzt, E. 2005 Mechanics of hierarchical adhesion structures of geckos. *Mech. Mater.* **37**, 275–285. (doi:10.1016/j.mechmat.2004.03.008)

Ge, L., Sethi, S., Ci, L., Ajayan, P. M. & Dhinojwala, A. 2007 Carbon nanotube-based synthetic gecko tapes. *Proc. Natl Acad. Sci. USA* **104**, 10 792–10 795. (doi:10.1073/pnas.0703505104)

Glassmaker, N. J., Jagota, A. & Hui, C. Y. 2005 Adhesion enhancement in a biomimetic fibrillar interface. *Acta Biomater.* **4**, 367–375. (doi:10.1016/j.actbio.2005.02.005)

Glassmaker, N. J., Jagota, A., Hui, C.-Y., Noderer, W. L. & Chaudhury, M. K. 2007 Biologically inspired crack trapping for enhanced adhesion. *Proc. Natl Acad. Sci. USA* **104**, 10 786–10 791. (doi:10.1073/pnas.0703762104)

Gorb, S., Varenberg, M., Peressadko, A. & Tuma, J. 2007 Biomimetic mushroom-shaped fibrillar adhesive microstructure. *J. R. Soc. Interface* **4**, 271–275. (doi:10.1098/rsif.2006.0164)

Greiner, C., Campo, A. D. & Arzt, E. 2007 Adhesion of bioinspired micropatterned surfaces: effects of pillar radius, aspect ratio, and preload. *Langmuir* **23**, 3495–3502. (doi:10.1021/la0633987)

Huber, G., Gorb, S., Spolenak, R. & Arzt, E. 2005 Resolving the nanoscale adhesion of individual gecko spatulae by atomic force microscopy. *Biol. Lett.* **1**, 2–4. (doi:10.1098/rsbl.2004.0254)

Hui, C.-Y., Glassmaker, N. J., Tang, T. & Jagota, A. 2004 Design of biomimetic fibrillar interfaces: 2. Mechanics of enhanced adhesion. *J. R. Soc. Interface* **1**, 35–48. (doi:10.1098/rsif.2004.0005)

Irschick, D. J., Austin, C. C., Petren, K., Fisher, R., Losos, J. B. & Ellers, O. 1996 A comparative analysis of clinging ability among pad-bearing lizards. *Biol. J. Linn. Soc.* **59**, 21–35.

Jagota, A. & Bennison, S. J. 2002 Mechanics of adhesion through a fibrillar microstructure. *Integr. Comp. Biol.* **42**, 1140–1145. (doi:10.1093/icb/42.6.1140)

Johnson, K. L., Kendall, K. & Roberts, A. D. 1971 Surface energy and the contact of elastic solids. *Proc. R. Soc. A* **324**, 301–313. (doi:10.1098/rspa.1971.0141)

Kim, S. & Sitti, M. 2006 Biologically inspired polymer microfibers with spatulate tips as repeatable fibrillar adhesives. *Appl. Phys. Lett.* **89**, 261 911. (doi:10.1063/1.2424442)

Kim, S., Aksak, B. & Sitti, M. 2007 Enhanced friction of elastomer microfiber adhesives with spatulate tips. *Appl. Phys. Lett.* **91**, 221 913. (doi:10.1063/1.2820755)

Liu, H. W. & Bhushan, B. 2003 Adhesion and friction studies of microelectromechanical systems/nanoelectromechanical systems materials using a novel microtriboapparatus. *J. Vacuum Sci. Technol. A* **21**, 1528–1538. (doi:10.1116/1.1560711)

Majidi, C. *et al.* 2006 High friction from a stiff polymer using microfiber arrays. *Phys. Rev. Lett.* **97**, 076 103. (doi:10.1103/PhysRevLett.97.076103)

Noderer, W. L., Shen, L., Vajpayee, S., Glassmaker, N. J., Jagota, A. & Hui, C.-Y. 2007 Enhanced adhesion and compliance of film-terminated fibrillar surfaces. *Proc. R. Soc. A* **463**, 2631–2654. (doi:10.1098/rspa.2007.1891)

Northen, M. T. & Turner, K. L. 2005 A batch fabricated biomimetic dry adhesive. *Nanotechnology* **16**, 1159–1166. (doi:10.1088/0957-4484/16/8/030)

Peressadko, A. & Gorb, S. N. 2004 When less is more: experimental evidence for tenacity enhancement by division of contact area. *J. Adhes.* **80**, 247–261. (doi:10.1080/00218460490430199)

Persson, B. N. J. & Gorb, S. 2003 The effect of surface roughness on the adhesion of elastic plates with application to biological systems. *J. Chem. Phys.* **119**, 11 437–11 444. (doi:10.1063/1.1621854)

Persson, B. N. J., Albohr, O., Tartaglino, U., Volokitin, A. I. & Tosatti, E. 2005 On the nature of surface roughness with application to contact mechanics, sealing, rubber friction and adhesion. *J. Phys. Condens. Matter* **17**, R1–R62. (doi:10.1088/0953-8984/17/1/R01)

Savkoor, A. R. & Briggs, G. A. D. 1977 The effect of tangential force on the contact of elastic solids in adhesion. *Proc. R. Soc. A* **356**, 103–114. (doi:10.1098/rspa.1977.0123)

Shen, L., Glassmaker, N. J., Jagota, A. & Hui, C.-Y. 2008 Strongly enhanced static friction using a film-terminated fibrillar interface. *Soft Matter* **4**, 618–625. (doi:10.1039/b714737f)

Spolenak, R., Gorb, S. & Arzt, E. 2005*a* Adhesion design maps for bio-inspired attachment systems. *Acta Biomater.* **1**, 5–13. (doi:10.1016/j.actbio.2004.08.004)

Spolenak, R., Gorb, S., Gao, H. & Arzt, E. 2005*b* Effects of contact shape on the scaling of biological attachments. *Proc. R. Soc. A* **461**, 305–319. (doi:10.1098/rspa.2004.1326)

Tang, T., Hui, C.-Y. & Glassmaker, N. J. 2005 Can a fibrillar interface be stronger and tougher than a non-fibrillar one? *J. R. Soc. Interface* **2**, 505–516. (doi:10.1098/rsif.2005.0070)

Tian, Y., Pesika, N., Zeng, H., Rosenberg, K., Zhao, B., McGuiggan, P., Autumn, K. & Israelachvili, J. 2006 Adhesion and friction in gecko toe attachment and detachment. *Proc. Natl Acad. Sci. USA* **103**, 19 320–19 325. (doi:10.1073/pnas.0608841103)

Timoshenko, S. P. & Gere, J. M. 1961 *Theory of elastic stability*, ch. 1. New York, NY: McGraw-Hill.

Varenberg, M. & Gorb, S. 2007 Shearing of fibrillar adhesive microstructure: friction and shear-related changes in pull-off force. *J. R. Soc. Interface* **4**, 721–725. (doi:10.1098/rsif.2007.0222)

Yao, H. & Gao, H. 2006 Mechanics of robust and releasable adhesion in biology: bottom-up designed hierarchical structures of gecko. *J. Mech. Phys. Solids* **54**, 1120–1146. (doi:10.1016/j.jmps.2006.01.002)

Yao, H., Della Rocca, G., Guduru, P. R. & Gao, H. 2007 Adhesion and sliding response of a biologically inspired fibrillar surface: experimental observations. *J. R. Soc. Interface* **5**, 723–733. (doi:10.1098/rsif.2007.1225)

Yurdumakan, B., Raravikar, N. R., Ajayan, P. M. & Dhinojwala, A. 2005 Synthetic gecko foothairs from multiwalled carbon nanotubes. *Chem. Commun.* **30**, 3799–3801. (doi:10.1039/b506047h)